scientific reports

Check for updates

OPEN

Modeling dry eye with an air–liquid interface in corneal epithelium-on-a-chip

Rodi Kado Abdalkader[1]✉, Romanas Chaleckis[2,3], Takuya Fujita[1,4] & Ken-ichiro Kamei[5,6,7]

Dry eye syndrome (DES) is a complex ocular condition characterized by an unstable tear film and inadequate tear production, leading to tissue damage. Despite its common occurrence, there is currently no comprehensive in vitro model that accurately reproduce the cellular characteristics of DES. Here we modified a corneal epithelium-on-a-chip (CEpOC) model to recapitulate DES by subjecting HCE-T human corneal epithelial cells to an air–liquid (AL) interface stimulus. We then assessed the effects of AL stimulation both in the presence and absence of diclofenac (DCF), non-steroidal anti-inflammatory drug. Transcriptomic analysis revealed distinct gene expression changes in response to AL and AL_DCF, affecting pathways related to development, epithelial structure, inflammation, and extracellular matrix remodeling. Both treatments upregulated *PIEZO2*, linked to corneal damage signaling, while downregulating *OCLN*, involved in cell–cell junctions. They increased the expression of inflammatory genes (e.g., *IL-6*) and reduced mucin production genes (e.g., *MUC16*), reflecting dry eye characteristics. Metabolomic analysis showed increased secretion of metabolites associated with cell damage and inflammation (e.g., methyl-2-oxovaleric acid, 3-methyl-2-oxobutanoic acid, lauroyl-carnitine) in response to AL and even more with AL_DCF, indicating a shift in cellular metabolism. This study showcases the potential use of AL stimulus within the CEpOC to induce cellular characteristics relevant to DES.

Dry eye syndrome (DES) is a prevalent and serious ocular condition that has a significant impact on the quality of life of affected patients. The condition is characterized by a range of symptoms, including ocular discomfort, inflammation, reduced visual acuity, and tear film instability, and its estimated prevalence varies between 20 and 30% depending on the population and diagnostic criteria used[1,2]. There are two main subtypes of DES, evaporative dry eye caused by decreased production of the lipid layer of the tear film and aqueous deficient dry eye caused by reduced production of the aqueous layer of the tear film[3,4]. The underlying causes of each subtype are complex and multifactorial, and include biological, environmental, and physiological factors[5].

Despite its prevalence and impact, the study of DES has been hindered by a lack of suitable in vitro models that can accurately capture the biological and biomechanical aspects of the disease. Conventional in vitro models such as cell culture inserts known as transwells, lack the capability to simulate the complex microenvironment of the ocular surface, underscoring the full understanding of disease progression and underlying mechanisms[6,7]. Additionally, in vivo animal models have limitations in their ability to provide insights into disease development similar to that in humans, owing to inter-species physiological variations[8,9].

To overcome these limitations, organ-on-a-chip (OoC) technology offers an appealing solution for the development of in vitro models[10]. OoC technology provides several advantages, including the ability to control cellular architecture and the capacity to recapitulate external stimuli such as air flow or liquid shear stress[10], which are essential factors in DES development.

We previously reported the development of a microfluidic device that was used as an OoC for growing corneal epithelial cells under the application of cycles of liquid stimuli for mimicking the eye blinking process[11]. Our previous studies have demonstrated the effectiveness of this technology in recapitulating tear movement

[1]Ritsumeikan Global Innovation Research Organization (R-GIRO), Ritsumeikan University, Shiga, Japan. [2]Gunma University Initiative for Advanced Research (GIAR), Gunma University, Maebashi, Japan. [3]Department of Occupational and Environmental Health, Nagoya City University Graduate School of Medical Sciences, Nagoya, Aichi, Japan. [4]Department of Pharmaceutical Sciences, Ritsumeikan University, Shiga, Japan. [5]Institute for Integrated Cell-Material Sciences (WPI-iCeMS), Kyoto University, Kyoto 606-8501, Japan. [6]Programs of Biology and Bioengineering, Divisions of Science and Engineering, New York University Abu Dhabi, Abu Dhabi, United Arab Emirates. [7]Department of Biomedical Engineering, Tandon School of Engineering, New York University, Brooklyn, NY 11201, USA. ✉email: rodi@fc.ritsumei.ac.jp

during eye blinking and providing temporal analysis of extracellular metabolites through a wide range of corneal transporters[12]. Moreover, OoC of the human cornea with a blinking lid was developed by a different group to model DES[13]. This was achieved by reducing the blinking rates, to allow a tear-like evaporation process; however, the specific mechanism concerning the changes in cell phenotypes under these conditions has not been fully addressed.

Considering that the pathology of corneal damage in evaporative DES is influenced by multiple factors, including tear film disturbances due to eye blinking and exposure to air. Therefore, creating a model that combines both air and liquid interfaces can potentially provide a more realistic representation of evaporative DES in the cornea. However, the extent to which the application of air–liquid stimuli in a microfluidic device can induce a DES-like phenotype in corneal epithelial cells remains unclear. Further investigation is necessary to address this question comprehensively and enhance our understanding of the effects of these stimuli on homeostasis of the corneal epithelium.

Here, we developed an air–liquid interface (AL) system within the CEpOC to mimic the DES-like cellular phenotype. Subsequently, we applied AL in combination with Diclofenac (DCF), a well-known non-steroidal anti-inflammatory drug with a controversial efficacy and safety profile in DES treatment[14–16]. To gain insights into the underlying molecular mechanism, we conducted a comprehensive dual-omics analysis, including RNA-sequencing (RNA-seq) of corneal epithelial cells and non-targeted LCMS-based analysis of extracellular metabolites collected spatiotemporally from microfluidic devices. Our research provides a better understanding of the cellular responses and metabolic changes associated with AL and with DCF treatment in the context of DES.

Results

Creating AL interface in microfluidic devices via CEpOC modification

We have made modifications to CEpOC device in order to generate AL stimuli. This entailed the creation of an AL interface within the microfluidic device. Our approach involved introducing a new component: an open reservoir with a diameter of 4 mm, positioned at the outlet area. For the generation of air source, we integrated a syringe pump with an air compressor tube. This tube branches into eight separate channels which are subsequently connected to each inlet of the microfluidic device. By employing negative and positive pressure, we were able to apply two cycles of stimuli. During the first cycle, air is introduced through the outlet (air infusion), where it effectively blends with the liquid present within the cell culturing channels. This establishes the initial conditions for generating the AL interface. In the subsequent cycle, the air is expelled, allowing for the replacement of the liquid (liquid infusion). Each cycle was applied for 10 s (air phase: 1 s, liquid phase: 1 s, pause phase: 8 s) (Fig. 1A,B). A visual representation of this process can be found in the supplementary figure (Supplementary Fig. 1A, B, C).

Constructing the corneal epithelial barrier in the modified CEpOC

To establish the corneal epithelial barrier, we followed our previously established protocol employing the human corneal epithelial cell line (HCE-T)[11]. The cells were cultivated for seven days, during which the formation of the epithelial barrier was established.

Confirmation of the epithelial barrier's presence was accomplished through immunofluorescence staining of the tight junction protein known as zonula occludens-1 (ZO-1), in conjunction with the visualization of actin fibers (F-actin). This indicated the formation of the barrier. Additionally, the cells exhibited other important characteristics, including the expression of the maturation marker cytokeratin 12 (CK12), along with the presence of the apical marker, P-glycoprotein 1 (P-gp) (Fig. 1C).

AL stimulus exhibits no significant impact on cell viability

To assess the effects of AL alone and in combination with DCF, we subjected the devices to AL stimulus cycles for a duration of 24 h (Fig. 1D(I)). Subsequently, we performed cell viability evaluations using Calcein AM staining, comparing the results with devices that were maintained under static control conditions with only the cell culturing medium. Our findings revealed that there was no significant decrease observed in cell viability presented in Calcein AM intensity under either AL or in the combination with DCF (AL_DCF). Although the cell area showed slight decrease under AL and AL_DCF conditions, these changes were not statistically significant (Fig. 1D(II)), E).

AL elicit transcriptomic changes related to corneal function, developmental process, and inflammatory pathways

To evaluate the impact of AL stimulus on corneal epithelial cells, we conducted RNA-seq analysis after subjecting the cells to either AL alone or in combination with DCF for 24 h (Fig. 2A(I)). To investigate the transcriptome changes that occur during the activation of biological pathways in response to different stimuli, we first performed cluster analysis of gene expression data. The results distinctly revealed alterations in gene expression patterns in response to AL stimuli alone or in combination with DCF, as compared to the control groups (ST and ST_DCF) (Fig. 2A(II)) (Supplementary Fig. 2).

To identify the differentially expressed genes (DEGs), we conducted a DEG analysis between the control groups (ST_DCF versus ST) and the experimental groups (AL versus ST and AL_DCF versus ST). In the DEG analysis of ST_DCF versus ST, we identified 274 DEGs, with 160 upregulated genes and 114 downregulated genes (Fig. 2B). The significantly upregulated genes were only annotated with the GO pathway of vitamin D 24-hydroxylase activity (GO:0070576) (Supplementary Fig. 3). In contrast, the DEG analysis of AL versus ST showed 1148 DEGs, with 417 upregulated genes and 731 downregulated genes (Fig. 2C). The significantly upregulated genes were annotated with GO pathways related to developmental processes (GO:0032502), anatomical structure development (GO:0048856), cell differentiation (GO:0030154), and cell adhesion (GO:0007155). The

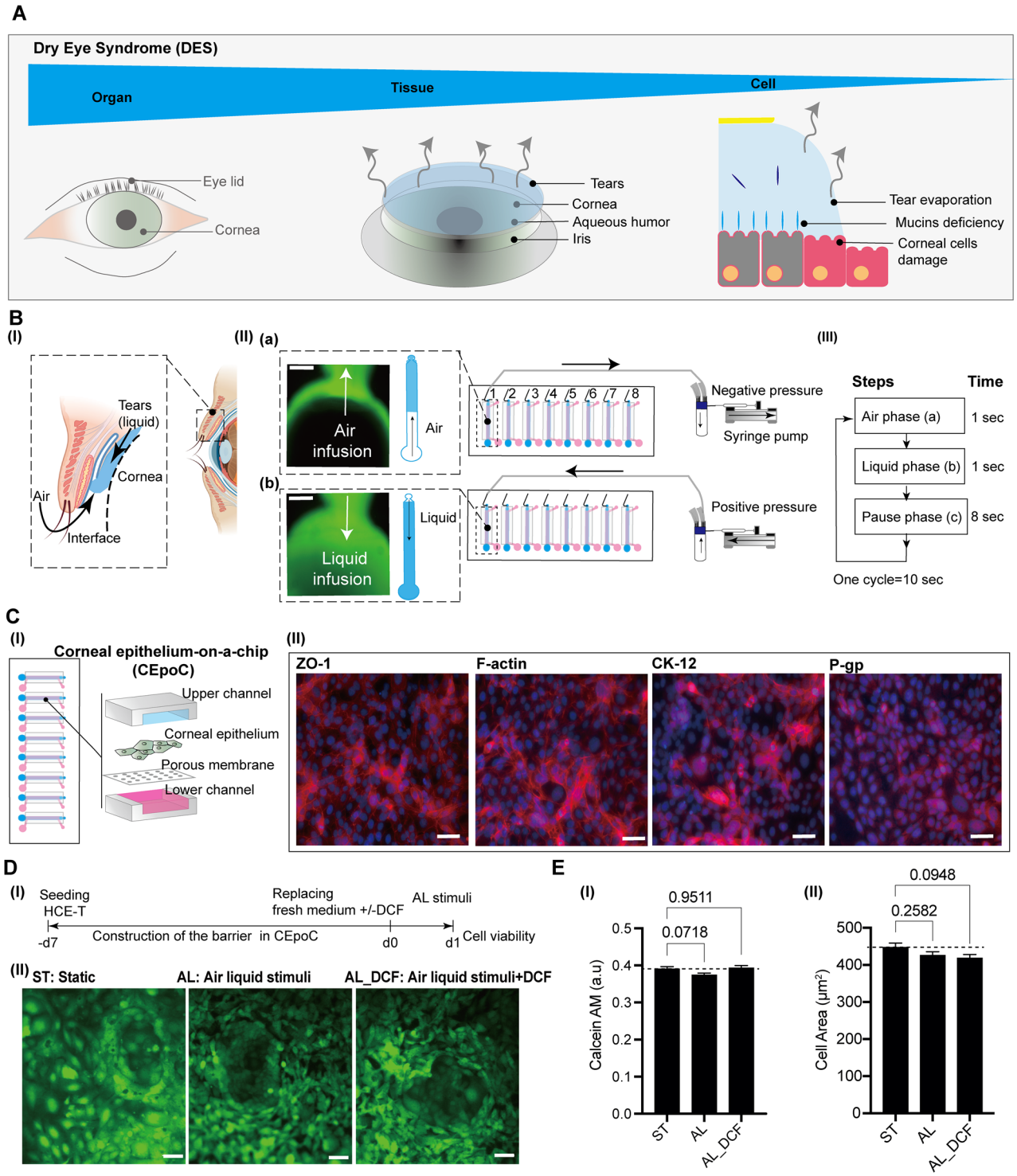

Figure 1. The conceptual design and characteristics of the modified CEpOC. (**A**) Schematic illustration showcases the evaporative dry eye. (**B**) The generation of AL stimulus in the modified CEpOC. I) Schematic illustration (created with BioRender.com) showcases air–liquid interphase process; II) The application of air–liquid stimuli in the microfluidic devices showcasing air infusion (a) then liquid infusion (b); III) The steps and duration of the application of air and liquid in the microfluidic device. Green color indicates the fluorescent signal of sodium fluorescein solution in the reservoir area. Scale bar, 500 μm. (**C**) I) Schematic illustration showcases the microfluidic device and HCE-T culturing for forming a barrier; II) Immunofluorescence staining of ZO-1, F-actin, CK12, and P-gp. Red color indicates the fluorescent signal of the targeted protein. Blue color indicates the nucleus satin DAPI. Scale bar, 50 μm. (**D**) Cell viability in the microfluidic devices under ST and AL conditions with and without DCF; I) The protocol that showcase HCE-T culturing, barrier formation and the AL stimuli; II) Microscopic images of Calcein-AM under ST and AL conditions with and without DCF. (**E**) Microscopic signal-cell analysis of Calcein-AM intensity (I) and cell area (II). The analysis was performed on images of independent samples; 1100 cells were randomly selected and analyzed for three independent samples. Green, Calcein-AM. Scale bar, 50 μm. Data are represented in the bar plot as means ± S.E.M. The *p*-values were determined by the Dunnett's multiple comparison test.

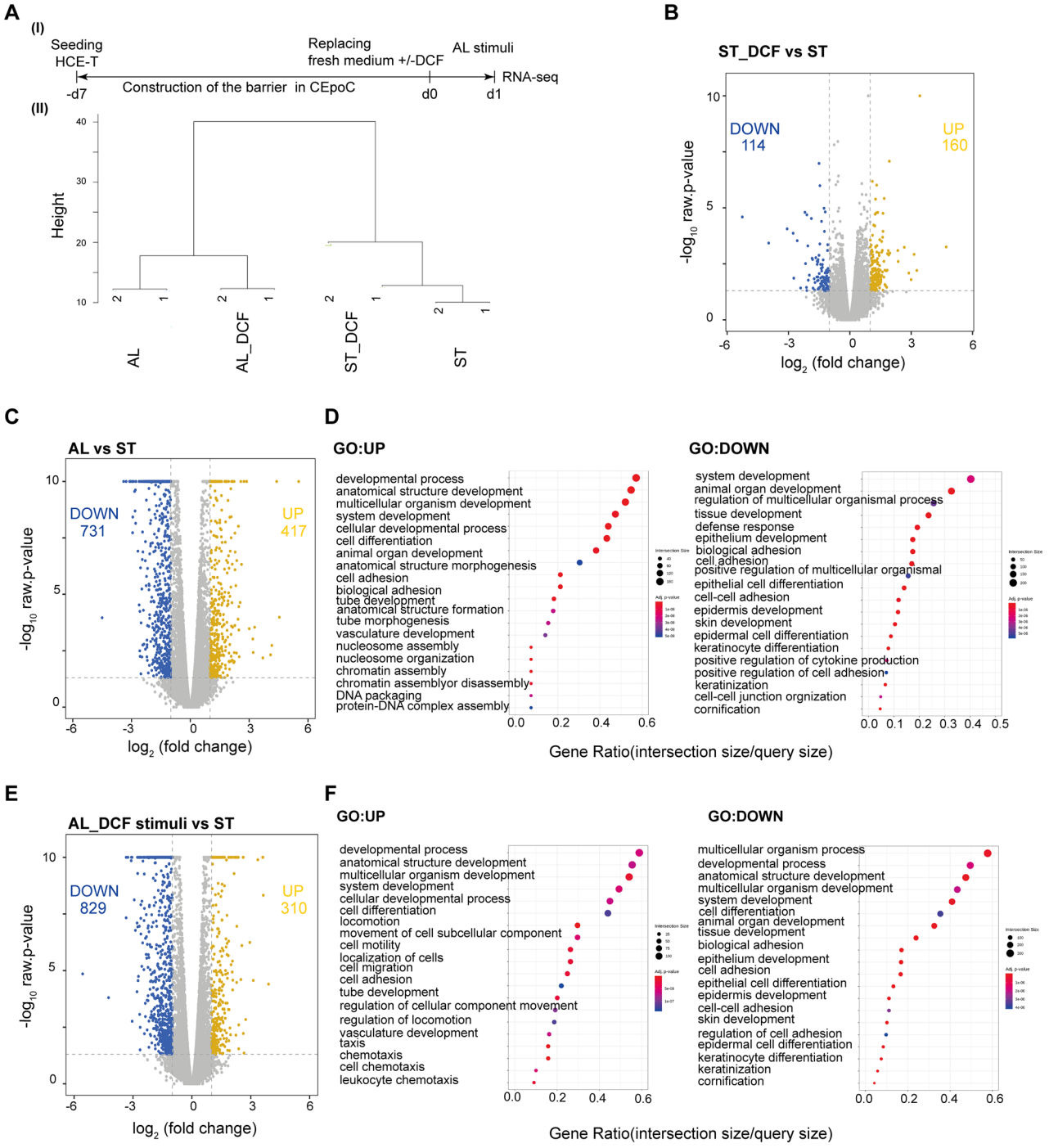

Figure 2. RNA-seq analysis of cells under AL stimulus. (**A**) I) The protocol that showcase the timeline of HCE-T culturing, barrier formation, and samples collection for RNA-seq; II) Dendrogram indicating the hierarchical clustering analysis, revealing the expression similarities among ST, ST_DCF, AL, and AL_DCF (Distance metric = Euclidean distance, Linkage method = Complete linkage). (**B**) The volcano plot representing the differentially expressed genes (DEGs) of ST_DCF versus ST. (**C**) The volcano plot representing the DEGs of AL versus ST. (**D**) GO pathways of DEGs in AL versus ST. (**E**) The volcano plot representing the DEGs of AL_DCF versus ST. (**F**) GO pathways of DEGs in AL_DCF versus ST. Genes with twofold change and p-value < 0.05 was applied. Blue: downregulated genes, yellow: upregulated genes.

downregulated genes were annotated with various GO pathways related to tissue development (GO:0009888), defense response (GO:0009653), epithelial development (GO:0060429), regulation of cytokine production (GO:0001819), keratinization (GO:0031424), and cornification (GO:0070268) (Fig. 2D) (Supplementary Fig. 4).

In the DEG analysis of AL_DCF versus ST, we identified 1139 DEGs, with 310 upregulated genes and 829 downregulated genes (Fig. 2E). The upregulated genes were annotated with GO pathways related to developmental processes (GO:0032502), anatomical structure development (GO:0048856), cell differentiation (GO:0030154), cell adhesion (GO:0007155), cell migration (GO:0016477), chemotaxis (GO:0006935), and leukocyte chemotaxis (GO:0030595). The downregulated genes were annotated with various GO pathways related to tissue development (GO:0009888), epithelial development (GO:0060429), keratinization (GO:0031424), and cornification (GO:0070268) (Fig. 2F) (Supplementary Fig. 5).

Our results revealed a significant alteration in the expression of mechanosensing markers. Notably, we observed an augmentation in the expression of *PIEZO2*, while concurrently noting a reduction in the expression levels of *TRPV3*, *TRPV6*, and *OCLN* in both the AL and AL_DCF. Furthermore, a significant decrease was observed in the expression of lubricant mucins markers (*MUC16*, *MUC20*, *MUC4*, *MUC2*, and *MUC6*) in both AL and AL_DCF. In contrast, a notable increase was observed in the expression of genes related to inflammation, extracellular matrix (ECM) remodeling, and disruption (*IL-6*, *CXCL2*, *CCL5*, *COL3A1*, *COL1A2*, *COL8A1*, *COL5A3*, *MMP1*, *MMP2*, and *MMP17*) in both AL and AL_DCF (Fig. 3A,B) (Supplementary Fig. 6).

The introduction of DCF did not reverse of the overexpression of *IL-6*, nor did it mitigate the reduction in the gene expression of mucin and occudens, as exemplified by *MUC1* and *MUC16*, and *OCLN* (Fig. 3B). Furthermore, the downregulation of the antioxidative enzyme related gene (*GSS*) remained unchanged despite the presence of DCF. However, it is noteworthy that the growth factor *TGFB1* transcript demonstrated a significant increase under AL stimuli. Intriguingly, this heightened expression was subsequently attenuated upon

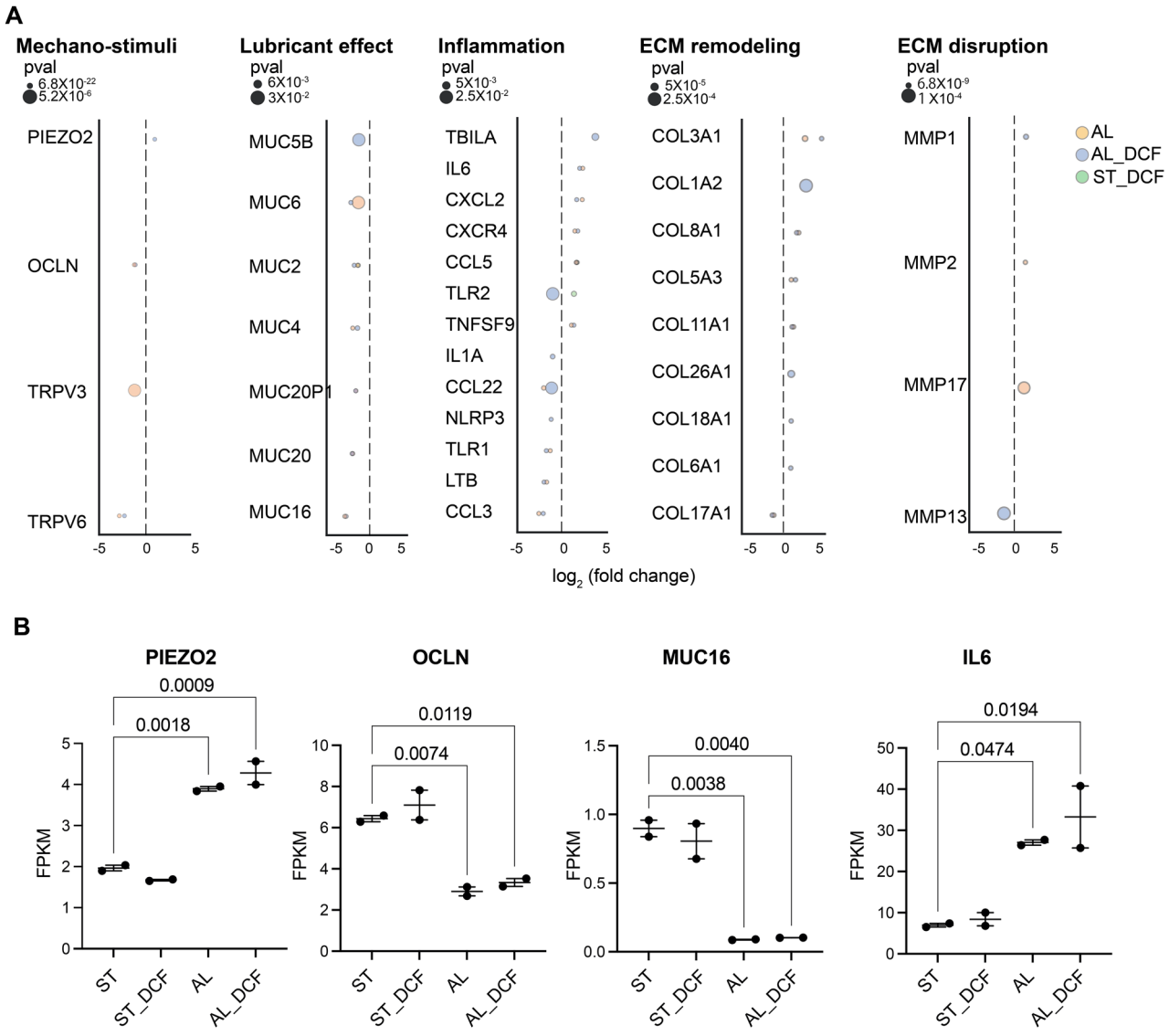

Figure 3. The impact of AL stimulus on the alteration of key DE-related transcripts. (**A**) DEGs of mechano-stimuli, lubricant effect, inflammation, ECM remodeling, and ECM disruption. Genes with twofold change and a p-value < 0.05 was applied. **(B)** The comparative gene expression (normalized FPKM values) of DES markers in HCE-T cells. Dot plot in which the mean of each group is indicated with a black line (data are presented in duplicates as means ± S.E.M). The p-values were determined by the Dunnett's multiple comparison test.

the addition of DCF in the AL_DCF treatment group (Supplementary Fig. 6). To investigate the impact of AL and AL_DCF on inducing any death signal in cells, we checked important genes related to apoptosis such as caspase-related genes (*CASP1*, *CASP2, CASP3, CASP4, CASP5, CASP6, CASP7, CASP8, CASP9, CASP10)* where there was no significant upregulation in these genes as compared with ST or ST_DCF (Supplementary Fig. 7).

AL elevates mitochondria-related metabolites

To investigate the impact of AL and AL_DCF in inducing change in the extracellular metabolites in both the apical (AP) and the basolateral (BA) compartments, LCMS-based none-targeted metabolomic analysis was performed at 0, 3, 6, and 24 h (Fig. 4A(I)). We were able to annotate a total of 121 metabolites (Supplementary data 1). We utilized peak areas for metabolite semi-quantification. The principal component analysis (PCA) results demonstrated a gradual shift in metabolite levels over time. This shift was evident from the systematic change in sample clusters at 3 h compared to 0 h, 6 h compared to 0 h, and 24 h compared to 0 h (Fig. 4A(II)). To identify unique metabolites, we employed partial least square discrimination analysis (PLS-DA) in combination with the variable importance in projection (VIP) (Fig. 4B). We considered metabolites with a score equal to or greater than 2. At 3 h, the identified metabolites included methyl-2-oxovaleric acid, 3-methyl-2-oxobutanoic acid, palmitoyl-carnitine, myristoyl-carnitine, hippuric acid, ureidopropionic acid, cytosine, and N, N-dimethylguanosine. At 6 h, the identified metabolites were stearoyl-carnitine, palmitoyl-carnitine, methyl-2-oxovaleric acid, 3-methyl-2-oxobutanoic acid, myristoyl-carnitine, and ureidopropionic acid. Finally, at 24 h, the identified metabolites were 3-methyl-2-oxobutanoic acid, methyl-2-oxovaleric acid, lauroyl-carnitine, decanoyl-carnitine, thiamine, and 3-hydroxyisovaleric acid. In addition, we investigated the translocation of DCF from the AP compartment into the BA compartment. We calculated the accumulation of DCF in the BA compartment over a 24 h period based on the AUC values. Our results revealed a rapid accumulation of DCF in the BA compartment within the first 6 h. However, after this initial period, we observed a saturation point where the accumulation of DCF reached a plateau and remained relatively stable up to 24 h (Supplementary Fig. 8A). We further investigated the permeation of DCF across the barrier toward the BA compartment within 3 h under both ST and AL conditions. The application of AL stimulus led to an increase in DCF permeation as compared to ST conditions, although these differences were not statistically significant (Supplementary Fig. 8B).

We subsequently directed our focus towards unique discovered metabolites, such as methyl-2-oxovaleric acid, 3-methyl-2-oxobutanoic acid, palmitoyl-carnitine, and decanoyl-carnitine. These metabolites were found to be secreted from both the AP and BA sides, albeit with distinct secretion kinetics.

To analyze the differences in secretion activity between AL and AL_DCF, we first adjusted the values based on channel volumes and then normalized them using the initial values at time 0. Next, we utilized the area under the curve (AUC) values to compare the metabolic activity. Under AL stimulation, both methyl-2-oxovaleric acid and 3-methyl-2-oxobutanoic were actively secreted from the AP side, exhibiting AUCs of 111.8 ± 10 and 124.8 ± 14, respectively. In comparison, their secretion activity on the BA side was lower, with AUCs of 44.79 ± 11 and 39.91 ± 11, respectively. Interestingly, the combination of AL with DCF enhanced the secretion of these metabolites on the AP side, resulting in increased AUCs of 151.6 ± 24 (methyl-2-oxovaleric acid) and 159 ± 30 (3-methyl-2-oxobutanoic acid). The elevation in secretion was accompanied by a slight increase in BA secretion as well, with AUCs of 55.71 ± 71 (methyl-2-oxovaleric acid) and 51.31 ± 8.6 (3-methyl-2-oxobutanoic acid) (Fig. 5A(I), A (II)).

On the contrary, in response to AL stimuli, lauroyl-carnitine and decanoyl-carnitine exhibited a tendency for active secretion on both the AP and BA sides, showing AUCs of 52.49 ± 13 and 55.63 ± 25 in BA side, respectively, in comparison to the AP side where their AUCs were 56.19 ± 3.7 (lauroyl-carnitine) and 36.79 ± 1.4 (decanoyl-carnitine). When combined with DCF, there was a slight increase in AP secretion, resulting in AUCs of 84.49 ± 11 (lauroyl-carnitine) and 82.2 ± 14 (decanoyl-carnitine). Also, there was a slight elevation in the secretion of lauroyl-carnitine in BA compartment (AUC:103.4 ± 22). However, decanoyl-carnitine did not show a notable change in secretion in the BA compartment (AUC: 55.26 ± 8) (Fig. 5A(II)). We further investigated genes with biological connections to these metabolites. For example, the Acetyl-CoA Acetyltransferase 1 (*ACAT1*) gene encodes an enzyme that catalyzes the breakdown of acetoacetate, a product of both methyl-2-oxovaleric acid and 3-methyl-2-oxobutanoic acid. Both AL and AL_DCF treatments led to a significant upregulation of this gene compared to the ST and ST_DCF treatments. Furthermore, we investigated the expression of Solute Carrier Family 16 Member 7 (*SLC16A7*) gene, that encode monocarboxylate transporter 2 and has an affinity for the ketone bodies such as acetoacetate and their derivatives (methyl-2-oxovaleric acid and 3-methyl-2-oxobutanoic acid). Interestingly, the expression level of *SLC16A7* gene was significantly upregulated under AL_DCF conditions (Fig. 5B). Additionally, we explored the expression of Carnitine Palmitoyltransferase 1A (*CPT1A*) gene, responsible for transferring long-chain fatty acids to carnitine, forming acylcarnitines such as lauroyl-carnitine and decanoyl-carnitine. We also investigated the Solute Carrier Family 25 Member 20 (*SLC25A20*) gene, which encodes a transporter accountable for conveying acylcarnitines across the mitochondrial membrane and governing mitochondrial oxidative metabolism. Our data reveals a noteworthy upregulation in the expression of *CPT1A* and *SLC25A20* genes under both AL and AL_DCF conditions as compared with ST and ST_DCF conditions. Notably, the AL_DCF group demonstrated a slightly diminished expression of *SLC25A20* (Fig. 5B).

Discussion

DES originates from various factors, such as the instability of the tear film and inadequate tear secretion. These factors expose the ocular surface to air, potentially resulting in tissue damage. To replicate the conditions of evaporative dry eye, we recognized the significance of applying an AL directly to the surface of the corneal epithelial barrier for inducing dry eye-like characteristics in cells. For this purpose, we employed our previously

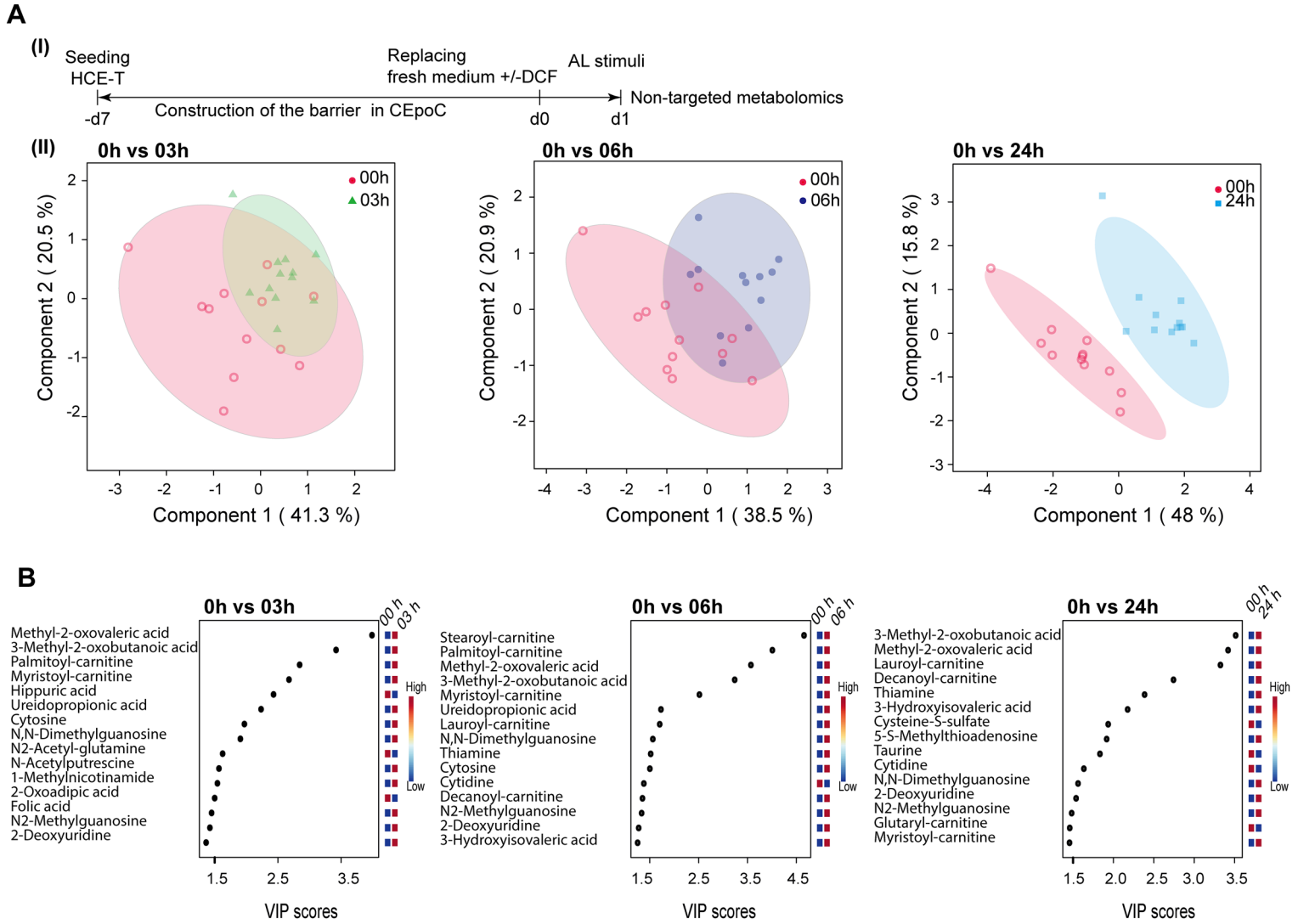

Figure 4. LCMS-based nontargeted metabolomic analysis of extracellular metabolites under AL stimulus. (**A**) I) The protocol that showcase the timeline of HCE-T culturing, barrier formation and extracellular samples collection (one microliter) for nontargeted metabolomics; II) Principal component analysis (PCA) of metabolomics dataset peak areas (log transformation) of samples (except internal standards, QC, and blanks) at 0 h versus 3 h, 0 h versus 6 h and 0 h versus 24 h, respectively. (**B**) Variable importance in projection (VIP) derived from the partial least square discrimination analysis (PLS-DA) that included all samples (except internal standards, QC, and blanks) for the selection of important metabolites at 0 h versus 3 h, 0 h versus 6 h and 0 h versus 24 h, respectively. p-value < 0.05 was applied.

A

(I)

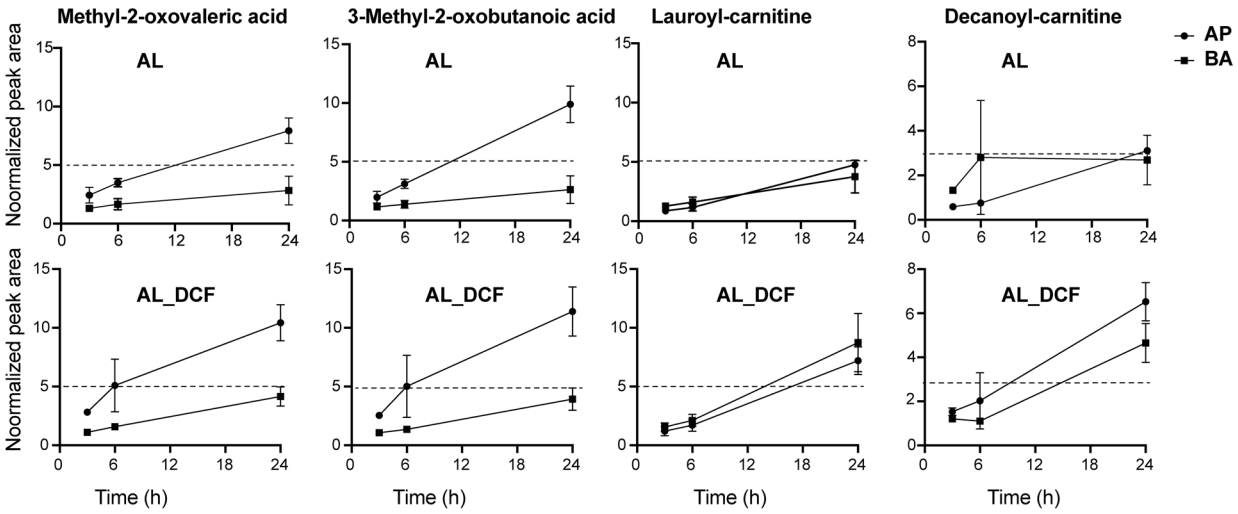

(II)

Metabolites	AP		BA	
	AUC	Std. Error	AUC	Std. Error
Methyl-2-oxovaleric acid_AL	111.8	10.39	44.79	11.84
Methyl-2-oxovaleric acid_AL_DCF	151.6	24.73	55.71	7.714
3-Methyl-2-oxobutanoic acid_AL	124.8	14.38	39.91	11
3-Methyl-2-oxobutanoic acid_AL_DCF	159	30.62	51.31	8.624
Lauroyl-carnitine_AL	56.19	3.713	52.49	13.01
Lauroyl-carnitine_AL_DCF	84.49	11.63	103.4	22.82
Decanoyl-carnitine_AL	36.79	1.473	55.63	25.47
Decanoyl-carnitine_ALDCF	82.2	14	55.26	8.032

B

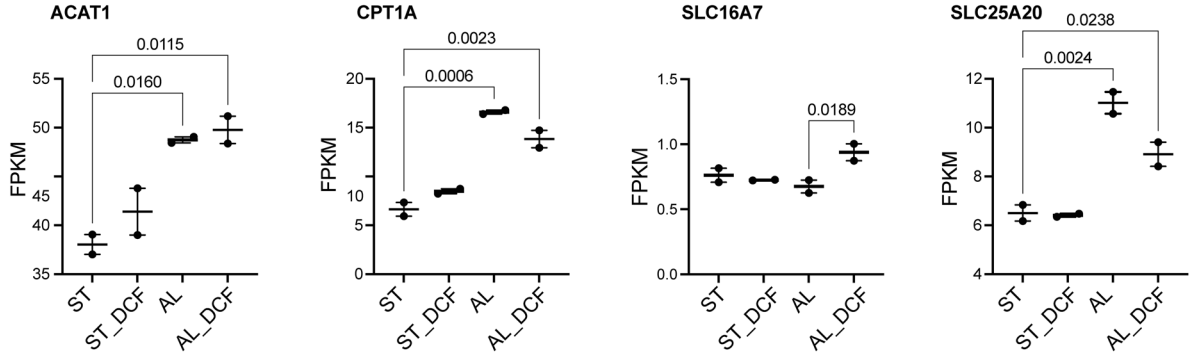

Figure 5. The effect of DCF on the alteration of extracellular metabolites under AL stimulus. (**A**) I) Selection of metabolites based on the VIP analysis score of highly active profile; under AL stimulus only (upper) and under AL stimulus and DCF treatment (lower). Peak areas were corrected by the channels volume and then normalized by the 0 h values. AP: apical, BA: basolateral. Data are presented in triplicates as means ± S.E.M. II) A table that summarizing the AUC values of metabolites from both AP and BA. (**B**) The comparative gene expression (normalized FPKM values) of essential metabolites-related genes in dot plot in which the mean of each group is indicated with a black line (data are presented in duplicates as means ± S.E.M). The *p*-values were determined using the Dunnett's multiple comparison test.

developed CEpOC with additional modifications such as a reservoir in the outlet area for increasing the exposure of air to cells periodically at regular intervals.

Our findings revealed that over the course of a week, HCE-T cells grew and expanded within the device, ultimately leading to the development of a barrier. The characteristics of the barrier was further verified through the observation of ZO-1 and other key markers such as P-gp and CK12. Collectively, these findings underscored the feasibility of creating a human corneal epithelial barrier within the adapted device.

We proceeded to apply the AL stimulus to the CEpoC for a duration of 24 h. We then assessed cell viability and morphology under two conditions: AL alone, and AL in combination with DCF (50 μM), as compared to cells under ST conditions. We decided the concentration of DCF of 50 μM as previously reported[14] , while a higher dose (200 μM) resulted in considerable cell death (data is not presented). Our results demonstrated that

the exposure to the AL stimulus did not lead to notable changes in cell viability, a conclusion supported by the Calcein AM intensity measurements. However, we noticed a modest decrease in cells area. It is worth noting that the use of DCF in the treatment of DES has generated conflicting outcomes in the literature. While it has been proposed as a potential treatment for DES where DCF has a protective effect against hyperosmolarity induced cell damage[14], there have been more contrasting reports highlighting cases of toxic reactions in corneal epithelial cells following DCF application[15–17]. In our results, we did not observe significant toxicity as determined by the Calcein AM assay.

To deepening our understanding about cell characteristics, we then investigated the transcriptomics alternation under AL and AL_DCF. We observed a distinct transcriptomic change between cells exposed to AL and AL_DCF conditions compared to those under ST and ST_DCF conditions, signifying a fundamental shift in the transcriptomic expression within the cells. Our analysis of GO pathways revealed significant impacts on processes related to development, anatomical structure formation, DNA packaging, epithelium development, cornification, and cell–cell junctions in both AL and AL_DCF conditions. Furthermore, the pathway related to chemotaxis and leukocyte chemotaxis was affected specifically in the AL_DCF group. Our data revealed an increase in genes associated with inflammation (such as *IL-6*) and a substantial decrease in genes linked to mucin production, notably *MUC16*. These results align with common observations in cases of DES. Furthermore, the AL stimulus elicited a noteworthy upregulation of *PIEZO2*, a mechanosensing channel expressed in the corneal epithelium[18], which could exacerbate the signaling of damage in DE patients[19]. Conversely, we observed a downregulation in the expression of *OCLN*, a gene related to cell–cell junctions. Although TRP channels, such as *TRPV3*, are expressed in the cornea and are associated with thermosensation[20], their contribution to DES is likely minor. As a result, we did not observe a significant increase in their expression in our data. Remarkably, these pathways collectively mirror common characteristics of biological pathways associated with DES, where disruptions to epithelial structure, compromised cell–cell junctions, the initiation of inflammatory responses, and the remolding of ECM are prevalent features[21,22]. Nevertheless, we did not detect any notable increase in the expression of the DES marker gene *MMP9*. MMP9 is known to be upregulated in response to active inflammation and acute injury[23]. Since the AL stimulus was applied for 24 h, it is plausible that our model captured the early stages of inflammation and tissue injury, thereby not demonstrating sufficient *MMP9* expression. Another consideration is that the AL stimulus was administered using a cell culture medium containing serum components essential for cell survival. However, the presence of serum might have an impact on the inflammatory process[24].

Non-targeted metabolomic analysis of DCF revealed a notable increase in DCF permeation across the epithelium barrier under AL stimulus compared to ST conditions after 3 h. These results support the transcriptomics analysis and cell morphology analysis, suggesting that AL stimulus could enhance DCF permeation, possibly due to the perturbation of tight junctions, as anticipated in DES conditions.

Furthermore, the non-targeted metabolomic analysis of extracellular samples revealed a systemic shift in metabolites over 24 h, indicating an alteration in the metabolic profile of cells. We observed a significant secretion of acylcarnitines in response to both AL and AL_DCF, consistent with our previous findings[12]. The carnitine shuttle plays a crucial role in facilitating the delivery of fatty acids into the mitochondria, initiating beta-oxidation and the tricarboxylic acid cycle, ultimately enhancing cellular energy production. SLC25 transporters are key players in this transportation process, actively contributing to the uptake and recycling of carnitine. In situations where fatty acid oxidation is impaired, the efflux of acylcarnitines from the mitochondria into the cytosol, and subsequently into the extracellular space, becomes crucial to prevent the accumulation of toxins within the mitochondria[25]. It is noteworthy that excessive secretion of acylcarnitines, such as lauroyl-carnitine, has been associated with inflammation[26]. Our results indicated an increase in the expression of *SLC25A20* under both AL and AL_DCF conditions. This suggests that *SLC25A20* may play a significant role in transporting these metabolites. Moreover, both methyl-2-oxovaleric acid and 3-methyl-2-oxobutanoic were prominently secreted apically, with higher levels observed in the AL_DCF condition. These metabolites are considered metabotoxins, suggesting an underlying disruption in cellular metabolism[27]. In our transcriptomic analysis, we observed a significant upregulation in the expression of *SLC16A7* gene, which encode monocarboxylate transporter 2 and has an affinity for acetoacetate and their derivatives metabolites (methyl-2-oxovaleric acid and 3-methyl-2-oxobutanoic)[28]. Considering the domination of the monocarboxylate transporters on the apical direction of the corneal epithelium[29], DCF might have an active impact of these transporters, leading to the excessive transportation of these metabolites in the apical direction. However, the precise mechanism favoring their apical release under DCF remains to be elucidated.

Collectively, our results suggest that AL stimulus enhances the secretion of metabolites indicative of cell damage and inflammation. This observation correlates with the upregulation of genes associated with inflammation (e.g., *IL-6*) and cellular damage (e.g., *OCLN* and *MUC16*). Interestingly, the addition of DCF does not appear to effectively mitigate these effects at the transcriptomic level and at the metabolomic level, potentially explaining the undefined outcomes observed in DES thus far. Notably, there is a slight downregulation of *TGFB1* gene expression under the combined influence of DCF and AL. Although, TGFB1 secretion is known to play a crucial role in cornea injury responses and the activation of keratinocytes in the corneal stroma[30], additional investigation is needed to determine whether the downregulation of *TGFB1* gene expression has any impact on DES.

Our study has several limitations. We focused on modeling the early stage of evaporative dry eye through the application of AL stimuli in CEpOC. To accurately replicate the later phases of the disease, which involve tissue inflammation and injury, it is important to consider additional elements such as incorporating immune cells and administrating chemical stimuli, such as TNF-a or IL-6 in combination with AL stimuli, in serum-free culturing conditions. Furthermore, an investigation into the protein secretome analysis, such as inflammatory cytokines and metalloprotease enzymes related to specific signaling pathways and mechanisms, is necessary. Additionally, future research should prioritize validating this model by using more clinically approved drugs. This validation will ensure the relevance and applicability of our model in a clinical context.

In conclusion, we examined how stimulating AL interface affects corneal epithelial cells in CEpOC with a purpose of mimicking conditions seen in evaporative dry eye. We successfully upregulated the CEpOC device to create an AL interface. By using HCE-T cells, we cultivated a corneal epithelial barrier within the modified CEpOC over a period of seven days. Transcriptomic analysis unveiled distinct patterns of gene expression in response to AL and AL_DCF stimuli. These changes were aligned with essential characteristics of DES, such as disrupted epithelial structure and inflammation. Metabolomic analysis revealed the secretion of group of metabolites, particularly acylcarnitines and metabotoxins, in response to AL and AL_DCF stimuli. Interestingly, DCF increased the apical secretion of these metabolites, which are associated with cellular damage and inflammation. Our study sheds light on the molecular and metabolic changes that underlie AL stimuli. The observed alterations suggest a cascade of events involving inflammation, disrupted cellular structure, and altered metabolism. Importantly, our findings raise questions about the effectiveness of DCF in mitigating these effects.

Methods

Microfluidic device fabrication

The microfluidic device was fabricated using stereolithographic 3D-printing techniques and solution cast-molding processes. Briefly, a mold for the microfluidic channels was produced using a 3D printer (Keyence Corporation, Osaka, Japan). Two molds were fabricated: upper blocks and lower blocks. Each block contained four chambers (15 mm length, 1.5 mm width, and 0.5 mm height). Prior to use, molds surfaces were coated with trichloro(1H,1H,2H,2H-perfluorooctyl) silane (Sigma-Aldrich, St. Louis, MO, USA). A Sylgard 184 PDMS two-part elastomer (ratio of 10:1 pre-polymer to curing agent; Dow Corning Corporation, Midland, MI, USA) was mixed, poured into the molds to produce a 4-mm-thick PDMS upper layer and a 0.5-mm-thick PDMS lower layer, and degassed using a vacuum desiccator for 1 h. The PDMS in the lower block was fixed on a glass slide. The PDMS material was then cured in an oven at 80 °C for 24 h. After curing, the PDMS was removed from the molds, trimmed, and cleaned. A clear polyester (PET) membrane (pore size of 0.4 µm, thickness 10 µm, nominal pore density of 4×10^6 pores cm^2) was fixed on each chamber of the lower PDMS block. Both PDMS blocks were corona-plasma-treated (Shinko Denki, Inc., Osaka, Japan) and bonded together by baking in an oven at 80 °C.

Human corneal epithelial cell culture

The human corneal epithelial cell line (HCE-T) was obtained from the RIKEN Bioresource Research Centre (Ibaraki, Japan). HCE-T cells were grown in a culture medium of DMEM/F12 supplemented with 5% fetal bovine serum, 5 µg/mL insulin, 10 ng/mL human epithelial growth factor, and 0.5% dimethyl sulfoxide, hereafter referred to as the cell growth medium. The cells were passaged at a ratio of 1:4 using trypsin–EDTA solution.

The construction of corneal epithelial barrier in the microfluidic device

Before use, the microfluidic cell culture device was sterilized by placing it under ultraviolet light in a biosafety cabinet for 30 min. The channels of the device were then washed with the DMEM/F12. Cells were harvested using trypsin and resuspended in the cell growth medium. The cell suspension was introduced into the upper channel of the device through a cell inlet with a cross-sectional area of 0.23 cm^2, at a density of 1×10^6 cells per mL. The microfluidic device was placed in a humidified incubator at 37 °C and5% CO^2 for 7 days, with the cell growth medium in each chamber being changed every 24 h.

The application of flow stimulus

Prior to the initiation of the AL stimulus, microfluidic channels were filled with fresh cell growth medium. For drug treatment with DCF, DCF was added to the upper channels at a final concentration of 50 µM, with a volume of 15 µL in the channel and 20 µL in the reservoir. The upper channels were exposed to the AL flow using a syringe pump (KD Scientific, Fisher scientific, Holliston, USA). Sterilized tubes (Tygon LMT-55) were divided into eight branches, which were then connected to an air reservoir tube. The entire setup was linked to a syringe pump that represented the source for negative and positive pressure in flow rate of 100 µL/s. Each air–liquid stimulus cycle had a duration of 10 s and consisted of three phases: Phase 1: air infusion phase for one second. Phase 2: liquid infusion for one second. Phase 3: a pause for 8 s under liquid static conditions. Throughout these phases, lower channels were maintained under static conditions.

The determination of cell viability

Cell viability was assessed by the live staining with Calcein AM (Dojindo Molecular Technologies, Inc.). Briefly, cells were incubated with Calcein AM at a final concentration of 10 µg mL^{-1} in cell growth medium at 37 °C for 60 min. The cells were then washed twice with PBS- and subjected to microscopic imaging.

Immunofluorescence and microscopic imaging

For the immunostaining, cells were fixed with 4% paraformaldehyde in PBS- for 25 min at 25 °C and then permeabilized with 0.5% Triton X-100 in PBS- for 10 min at 25 °C. Subsequently, cells were blocked with blocking buffer (5% (v/v) bovine serum albumin, 0.1% (v/v) Tween-20) at 25 °C for 1 h and then incubated at 4 °C for overnight with the primary antibody in blocking buffer (Supplementary Table 1). Cells were then incubated at 37 °C for 60 min with a secondary antibody (Alexa Fluor 594 donkey anti-rabbit IgG and Alexa Fluor 594 donkey anti-mouse IgG 1:1000; Jackson ImmunoResearch, West Grove, PA, USA) in blocking buffer prior to a final incubation with 4′,6-diamidino-2-phenylindole (DAPI) or anti-phalloidin for F-actin at 25 °C. For imaging, we used a Nikon ECLIPSE Ti inverted fluorescence microscope equipped with a CFI plan fluor 10 × /0.30 N.A. objective lens (Nikon, Tokyo, Japan). Images were then analyzed using ImageJ software (National Institute of Health,

Maryland, USA). The analysis of single-cell data for Calcein AM was conducted using Cell Profiler software[31] (Version 3.1.8; Broad Institute of Harvard and MIT, USA). Random images were selected from independent biological triplicate samples, and the analysis followed a two-step pipeline provided by the software. In the first step, primary nucleus objects were identified through either auto or Otsu segmentation, based on their diameter and fluorescence intensity. Subsequently, the fluorescent mean intensity and morphological characteristics were calculated and exported for further analysis and plotting.

RNA extraction and sequencing

RNA extracted using RNeasy Mini Kit (Qiagen, Hilden, Germany) according to the maker instruction. Samples quality was assured by using the bioanalyzer (Agilent technologies, Inc., USA) with an RNA Integrity Number (RIN) value greater than or equal or higher than 7. Samples were then applied for the next generation sequencing (Macrogen, Tokyo, Japan) starting with RNA-seq library construction (TruSeq stranded mRNA LT Sample Prep Kit) followed by sequencing by NovaSeq 6000 Illumina system using 101 reads per specimen.

RNA-seq data mining and GO enrichment analysis

The quality control of the sequenced raw reads was performed by calculating overall reads quality, total bases, total reads, GC (%) and basic statistics (FastQC v0.11.7). In order to reduce biases in analysis, artifacts such as low-quality reads, adaptor sequence, contaminant DNA, or PCR duplicates were removed (Trimmomatic0.38)[32]. Trimmed reads were mapped to reference genome with HISAT2, splice-aware aligner (HISAT2 version 2.1.0, Bowtie2 2.3.5.1)[33,34]. Transcript was assembled by StringTie with aligned reads (StringTie version 2.1.3b)[35]. This process provided information of known transcripts, novel transcripts, and alternative splicing transcripts. Expression profiles were represented as read count and normalization value which is based on transcript length and depth of coverage. The FPKM (Fragments Per Kilobase of transcript per Million Mapped reads) value or the RPKM (Reads Per Kilobase of transcript per Million Mapped reads) is used as a normalization value. Differentially Expressed Genes (DEG) analysis was conducted using read count values obtained from StringTie. Initially, low-quality transcripts were filtered out during data preprocessing. Then, (Trimmed Mean of M-values) TMM normalization was applied. For statistical analysis, Fold Change and exact Test from edgeR were employed for each comparison pair. Significant results were identified based on the criteria of $|\text{Fold Change}| >= 2$ and an exact Test raw p-value < 0.05. Enrichment test was conducted with significant gene list using g:Profiler tool platform[36].

Extracellular metabolites collection and analysis by LCMS

One microliter of extracellular samples was collected as previously reported[12,37,38]. Tubes containing one microliter of dried extracellular samples were thawed and 150 µL of water and acetonitrile (3:7, v/v) was added, containing three technical internal standards (tISs): 0.1 µM CHES, 0.1 µM HEPES, and 0.2 µM PIPES. After resuspension, all samples were centrifuged at room temperature for 1 min at 1000 × g. A quality control (QC) sample was prepared by pooling an aliquot from each sample. Next, 40 µL of the supernatant was transferred to a 96-well 0.2 mL PCR plate (PCR-96-MJ; BMBio, Tokyo, Japan). The plate was sealed with a pierceable seal (4titude; Wotton, UK) for 3 s at 180 °C using a plate sealer (PX-1; Bio-Rad, Hercules, CA, USA) and maintained at 10 °C during the LCMS measurements. The LCMS method has been described previously[39]. The injection volumes were 7 µL in negative and 3 µL in positive ionization mode. In brief, metabolite separation was achieved on an Agilent 1290 Infinity II system using a SeQuant ZIC-HILIC (Merck, Darmstadt, Germany) column and a gradient between water containing 0.1% formic acid (pH = 2.6) and acetonitrile containing 0.1% formic acid in positive ionization mode, and a SeQuant ZIC-pHILIC (Merck, Darmstadt, Germany) column and a gradient of acetonitrile and 5 mM ammonium acetate in water (pH = 9.3) in negative ionization mode. Data were acquired on an Agilent 6550 Q-TOF–MS system with a mass range of 40–1200 m/z in all ion fragmentation mode, including three sequential experiments at alternating collision energies: full scan at 0 eV, followed by MS/MS scans at 10 eV and 30 eV, with a data acquisition rate of 6 scans/s. Data were converted to mzML format using Proteowizard and processed using MS-DIAL version 4.80[40–42] An in-house library containing accurate masses (AMs) and retention times (RTs) for 622 compounds obtained from chemical standards was used to annotate the detected compounds. Peak areas exported from MS-DIAL were used for metabolites' semi-quantification. Only metabolites with a coefficient of variation (CV) less than 30% in the QC samples or D-Ratio[43] < 50 were used for further analysis.

Data visualization and statistics

Data are represented as mean ± S.E.M. RNA-seq data are presented in duplicate of independent biological samples. Other data are presented of triplicate or more of independent biological samples. The unpaired t-test, Tukey's, Dunnett multiple comparison test were performed using GraphPad prism 8 (GraphPad Software, La Jolla California, USA). Principal component analysis (PCA) visualization was performed using the MetaboAnalyst platform[44]. Orange 3 software (Version 3.23.1; Bioinformatics Laboratory, Faculty of Computer and Information Science, University of Ljubljana, Slovenia) were used for data mining. Python Jupyter notebook 6.1.4, with Pandas and Bioinfokit packages. Data visualization was performed using Python 3 with matplotlib and seaborn packages.

Data availability

RNA-seq data have been deposited to the GEO repository under GEO accession number GSE244787.

Received: 11 October 2023; Accepted: 15 February 2024
Published online: 20 February 2024

References

1. Papas, E. B. The global prevalence of dry eye disease: a bayesian view. *Ophthalmic Physiol. Opt.* **41**, 1254–1266 (2021).
2. Moss, S. E. Prevalence of and risk factors for dry eye syndrome. *Arch. Ophthalmol.* **118**, 1264 (2000).
3. Lemp, M. A., Crews, L. A., Bron, A. J., Foulks, G. N. & Sullivan, B. D. Distribution of aqueous-deficient and evaporative dry eye in a clinic-based patient cohort. *Cornea* **31**, 472–478 (2012).
4. Crespo-Treviño, R. R., Salinas-Sánchez, A. K., Amparo, F. & Garza-Leon, M. Comparative of meibomian gland morphology in patients with evaporative dry eye disease versus non-dry eye disease. *Sci. Rep.* **11**, 20729 (2021).
5. Lemp, M. A. *et al.* The definition and classification of dry eye disease: Report of the definition and classification subcommittee of the international dry eye workshop (2007). *Ocul. Surf.* **5**, 75–92 (2007).
6. Reichl, S. Human corneal equivalent as cell culture model for in vitro drug permeation studies. *Br. J. Ophthalmol.* **88**, 560–565 (2004).
7. Wilson, S. L., Ahearne, M. & Hopkinson, A. An overview of current techniques for ocular toxicity testing. *Toxicology* **327**, 32–46 (2015).
8. Huh, D., Hamilton, G. A. & Ingber, D. E. From 3D cell culture to organs-on-chips. *Trends Cell Biol.* **21**, 745–754 (2011).
9. Seifirad, S. & Haghpanah, V. Inappropriate modeling of chronic and complex disorders: How to reconsider the approach in the context of predictive, preventive and personalized medicine, and translational medicine. *EPMA J.* **10**, 195–209 (2019).
10. Leung, C. M. *et al.* A guide to the organ-on-a-chip. *Nat. Rev. Methods Prim.* **2**, 33 (2022).
11. Abdalkader, R. & Kamei, K.-I. Multi-corneal barrier-on-a-chip to recapitulate eye blinking shear stress forces. *Lab Chip* **20**, 1410–1417 (2020).
12. Abdalkader, R., Chaleckis, R., Wheelock, C. E. & Kamei, K. Spatiotemporal determination of metabolite activities in the corneal epithelium on a chip. *Exp. Eye Res.* **209**, 108646 (2021).
13. Seo, J. *et al.* Multiscale reverse engineering of the human ocular surface. *Nat. Med.* **25**, 1310–1318 (2019).
14. Sawazaki, R. *et al.* Diclofenac protects cultured human corneal epithelial cells against hyperosmolarity and ameliorates corneal surface damage in a rat model of dry eye. *Invest. Ophthalmol. Vis. Sci.* **55**, 2547–2556 (2014).
15. Lee, J. S., Kim, Y. H. & Park, Y. M. The toxicity of nonsteroidal anti-inflammatory eye drops against human corneal epithelial cells in vitro. *J. Korean Med. Sci.* **30**, 1856 (2015).
16. Gronert, K. *et al.* Long-term use of diclofenac exacerbates immune driven dry eye disease by inhibiting lipoxin A4 formation in lymph nodes and lacrimal glands. *Invest. Ophthalmol. Vis. Sci.* **56**, 289–289 (2015).
17. Gokhale, N. S. & Vemuganti, G. K. Diclofenac-induced acute corneal melt after collagen crosslinking for Keratoconus. *Cornea* **29**, 117–119 (2010).
18. Morozumi, W. *et al.* Piezo channel plays a part in retinal ganglion cell damage. *Exp. Eye Res.* **191**, 107900 (2020).
19. Yang, S., Wu, Y., Wang, C. Y. & Jin, X. Ocular surface ion-channels are closely related to dry eye: Key research focus on innovative drugs for dry eye. *Front. Med.* **9**, 830853 (2022).
20. Yamada, T. *et al.* Functional expression of transient receptor potential vanilloid 3 (TRPV3) in corneal epithelial cells: Involvement in thermosensation and wound healing. *Exp. Eye Res.* **90**, 121–129 (2010).
21. Efraim, Y. *et al.* Alterations in corneal biomechanics underlie early stages of autoimmune-mediated dry eye disease. *J. Autoimmun.* **114**, 102500 (2020).
22. Zhang, Y. *et al.* Hyperosmolarity disrupts tight junction via TNF-α/MMP pathway in primary human corneal epithelial cells. *Int. J. Ophthalmol.* **15**, 683 (2022).
23. Shetty, R. *et al.* Elevated expression of matrix metalloproteinase-9 and inflammatory cytokines in keratoconus patients is inhibited by cyclosporine A. *Investig. Ophthalmol. Vis. Sci.* **56**, 738–750 (2015).
24. Santos, L. M., Cardoso, P. E. S., Diniz, E. A., Rahhal, J. G. & Sipert, C. R. Different concentrations of fetal bovine serum affect cytokine modulation in Lipopolysaccharide-activated apical papilla cells in vitro. *J. Appl. Oral Sci.* **31**, e20230020 (2023).
25. Kunji, E. R. S., King, M. S., Ruprecht, J. J. & Thangaratnarajah, C. The SLC25 carrier family: Important transport proteins in mitochondrial physiology and pathology. *Physiology* **35**, 302–327 (2020).
26. Sampey, B. P. *et al.* Metabolomic profiling reveals mitochondrial-derived lipid biomarkers that drive obesity-associated inflammation. *PLoS One* **7**, e38812 (2012).
27. Chashmniam, S. *et al.* A pilot study of the effect of phospholipid curcumin on serum metabolomic profile in patients with non-alcoholic fatty liver disease: A randomized, double-blind, placebo-controlled trial. *Eur. J. Clin. Nutr.* **73**, 1224–1235 (2019).
28. Bröer, S. *et al.* Characterization of the high-affinity monocarboxylate transporter MCT2 in Xenopus laevis oocytes. *Biochem. J.* **341**, 529 (1999).
29. Sun, Y.-C., Liou, H.-M., Yeh, P.-T., Chen, W.-L. & Hu, F.-R. Monocarboxylate transporters mediate fluorescein uptake in corneal epithelial cells. *Investig. Opthalmol. Vis. Sci.* **58**, 3716 (2017).
30. Tandon, A., Tovey, J. C. K., Sharma, A., Gupta, R. & Mohan, R. R. Role of transforming growth factor beta in corneal function, biology and pathology. *Curr. Mol. Med.* **10**, 565–578 (2010).
31. McQuin, C. *et al.* Cell Profiler 3.0: Next-generation image processing for biology. *PLOS Biol.* **16**, e2005970 (2018).
32. Bolger, A. M., Lohse, M. & Usadel, B. Trimmomatic: A flexible trimmer for Illumina sequence data. *Bioinformatics* **30**, 2114–2120 (2014).
33. Kim, D., Langmead, B. & Salzberg, S. L. HISAT: A fast spliced aligner with low memory requirements. *Nat. Methods* **12**, 357–360 (2015).
34. Li, H. *et al.* The sequence alignment/map format and SAMtools. *Bioinformatics* **25**, 2078–2079 (2009).
35. Pertea, M. *et al.* StringTie enables improved reconstruction of a transcriptome from RNA-seq reads. *Nat. Biotechnol.* **33**, 290–295 (2015).
36. Raudvere, U. *et al.* g:Profiler: A web server for functional enrichment analysis and conversions of gene lists (2019 update). *Nucleic Acids Res.* **47**, W191–W198 (2019).
37. Abdalkader, R., Chaleckis, R. & Fujita, T. Early differentiation signatures in human induced pluripotent stem cells determined by non-targeted metabolomics analysis. *Metabolites* **13**, 706 (2023).
38. Abdalkader, R. *et al.* Untargeted LC-MS metabolomics for the analysis of micro-scaled extracellular metabolites from hepatocytes. *Anal. Sci.* **37**, 1049–1052 (2021).
39. Meister, I. *et al.* High-precision automated workflow for urinary untargeted metabolomic epidemiology. *Anal. Chem.* **93**, 5248–5258 (2021).
40. Chambers, M. C. *et al.* A cross-platform toolkit for mass spectrometry and proteomics. *Nat. Biotechnol.* **30**, 918–920 (2012).
41. Tsugawa, H. *et al.* MS-DIAL: Data-independent MS/MS deconvolution for comprehensive metabolome analysis. *Nat. Methods* **12**, 523–526 (2015).
42. Tsugawa, H. *et al.* A lipidome atlas in MS-DIAL 4. *Nat. Biotechnol.* **38**, 1159–1163 (2020).
43. Broadhurst, D. *et al.* Guidelines and considerations for the use of system suitability and quality control samples in mass spectrometry assays applied in untargeted clinical metabolomic studies. *Metabolomics* **14**, 72 (2018).
44. Chong, J. *et al.* MetaboAnalyst 4.0: Towards more transparent and integrative metabolomics analysis. *Nucleic Acids Res.* **46**, W486–W494 (2018).

Acknowledgements
Funding was generously provided by the Japan Society for the Promotion of Science (JSPS, 22K14548 and JSPS, 20KK0160), and the Hirose Foundation to Rodi Kado Abdalkader. We acknowledge the WPI-iCeMS supported by the World Premier International Research Centre Initiative (WPI), the Ritsumeikan Global Innovation Research Organization (R-GIRO) and Gunma University Initiative for Advanced Research (GIAR) for their support. Author Rodi Kado Abdalkader—Earlier known as Rodi Abdalkader

Author contributions
R.K.A. took responsibility for the overarching research concept, project management, biological experiment design and execution, data analysis and interpretation, results visualization, and manuscript writing. R.C. conducted the nontargeted metabolomic LCMS analysis, contributing to data interpretation and manuscript refinement. K.K. and T.F. provided resources and contributed to data interpretation and manuscript improvement. All authors have reviewed and approved the final version of the manuscript for publication.

Competing interests
The authors declare no competing interests.

Additional information
Supplementary Information The online version contains supplementary material available at https://doi.org/10.1038/s41598-024-54736-z.

Correspondence and requests for materials should be addressed to R.K.A.

Reprints and permissions information is available at www.nature.com/reprints.

Publisher's note Springer Nature remains neutral with regard to jurisdictional claims in published maps and institutional affiliations.